

Fast whole-brain imaging of seizures in zebrafish larvae by two-photon light sheet microscopy

Giuseppe de Vito^{1,2,†}, Lapo Turrini^{2,3,†}, Caroline Müllenbroich^{2,4,5}, Pietro Ricci², Giuseppe Sancataldo^{2,3}, Giacomo Mazzamuto^{2,5}, Natascia Tiso⁶, Leonardo Sacconi^{2,5}, Duccio Fanelli³, Ludovico Silvestri^{2,3,5}, Francesco Vanzi^{2,7}, Francesco Saverio Pavone^{2,3,5,*}.

1 University of Florence, Department of Neuroscience, Psychology, Drug Research and Child Health, Viale Pieraccini 6, Florence, Italy, 50139

2 European Laboratory for Non-Linear Spectroscopy, Via Nello Carrara 1, Sesto Fiorentino, Italy, 50019

3 University of Florence, Department of Physics and Astronomy, Via Sansone 1, Sesto Fiorentino, Italy, 50019

4 School of Physics and Astronomy, Kelvin Building, University of Glasgow, G12 8QQ, Glasgow, UK

5 National Institute of Optics, National Research Council, Via Nello Carrara 1, Sesto Fiorentino, Italy, 50019

6 University of Padova, Department of Biology, Via U. Bassi 58/B, Padua, Italy, 35131

7 University of Florence, Department of Biology, Via Madonna del Piano 6, Sesto Fiorentino, Italy, 50019

**francesco.pavone@unifi.it*

†these authors contributed equally to this work

Abstract

Deciphering the workings of a brain (and its alterations due to pathologies and disorders) requires real-time mapping of the activity of all neurons. Recently, this formidable task has been brought into reach by the implementation of light sheet fluorescence (LSF) microscopy on the transparent zebrafish larva, a simple yet representative model of the vertebrate brain.

This application is however hindered by the use of visible light for fluorescence excitation, inducing unwanted visual stimulation that can only be partially overcome resorting to complex excitation geometries. On the other hand, two-photon (2P) LSF microscopy, owing to the use of invisible infra-red illumination, enables volumetric imaging of neuronal activity avoiding undesirable visual stimulation. However, due to the low efficiency of the 2P absorption process, the imaging speed of this technique is typically limited (~ 1 Hz) by the signal to noise ratio achievable without sample photodamage.

Here we describe a custom-made 2P LSF microscope that overcomes this limit, being specifically designed to perform whole-brain cellular-resolution calcium imaging in zebrafish larvae quintuplicating previous volumetric acquisition frequency (5 Hz). This result has been achieved by alternating the illumination of the two halves of the field-of-view to maximize the peak power of excitation light, by controlling the excitation light polarisation to orient the emission toward the detection objective, by employing a remote focussing approach to enable signal collection with a high-numerical aperture immersion objective without generating pressure waves on the sample, and by optically demagnifying the images on the detector sensor to decrease readout and integration times.

We employed this system to investigate, in real-time on a brain-wide scale, the onset and propagation of acute seizures, as induced by the convulsant drug pentylenetetrazol (PTZ), avoiding detrimental visual stimulation on a highly susceptible system such as an epileptic brain. At a moderate PTZ concentration we observed a widespread increase in nervous activity synchronization with the progression of the exposure time to the drug, particularly in the optic tectum, associated with an unexpected synchronization decrease happening in small spatially-defined areas. At saturating PTZ concentrations we instead observed a brain-wide functional connectivity reorganization and the emergence of distinctive phases of ictal and postictal activity. During the ictal phase the degree of synchronization in the neuronal activity dramatically increases in the whole-brain. On the contrary, the degree of neuronal synchrony in the postictal phase resembles the control condition, with the exception of the dorsal thalamus, where it increases, and subregions of the spinal cord, where it unexpectedly decreases.

The volumetric frame rate of our system allowed us to observe the emergence of previously unreported fast rhythmic ictal waves propagating in postero-anterior direction, which we termed caudo-rostral ictal waves (CRIWs), spanning across the whole larval encephalon in about 1 s during the ictal phase.

In conclusion, the presented 2P LSF microscope design affords high spatio-temporal resolution while avoiding visual stimuli and allows unprecedented access to whole zebrafish brain epileptic dynamics.

Introduction

Recent scientific advances, both in microscopy technology^{1–5} and in fluorescent sensors of neuronal activity^{6,7}, have led to a profound revolution in the field of brain functional imaging, making it pivotal for understanding brain functions. In this scenario, light sheet fluorescence microscopy (LSFM)⁸ plays a crucial role. Indeed, owing to its unique architecture, which couples optical sectioning ability with parallelization of the acquisition process within each frame, LSFM has allowed for the first time the high-speed volumetric imaging of a vertebrate brain in its entirety⁹. Actually, when applied to intrinsically transparent zebrafish larvae expressing fluorescent calcium indicators, this technique enabled the real-time investigation of large populations of neurons, leading to novel insights into circuit dynamics^{10–14}. Conventional LSFM employs one-photon (1P) lasers as excitation sources and, apart from the use of peculiar illumination schemes aimed at tailoring the incoming beams to exclude eye exposure¹⁵, this usually leads to detrimental visual stimulation during the acquisition process. At best, the use of a visible light sheet may induce undesired activation of retino-recipient neurons throughout the brain, making it hard to disentangle this activity from the one of interest. At worst, it may preclude neuronal activity investigation in more delicate experimental conditions, i.e. more susceptible to photostimulation, such as target-driven fictive navigation, sleep/wake rhythm or specific pathological states.

The use of two-photon (2P) excitation¹⁶ instead, employing near infrared (IR) pulsed light, which is invisible to the majority of vertebrates (zebrafish included^{17,18}), allows for a potential expansion of the experimental panorama amenable to high-speed imaging. However, owing to the low probability of the 2P absorption process, 2P

LSFM is prone to low signal-to-noise ratio (SNR) issues, which remarkably limit the actual volumetric acquisition speed¹⁹. For this reason, so far, 2P LSFM has been proficiently applied to perform structural studies²⁰, single plane functional imaging^{21,22} and proof-of-principle functional studies at low volumetric rate²³. To date, no high-speed volumetric functional imaging was performed by means of 2P LSFM. Here we describe a novel custom-made 2P LSFM setup optimized for fast whole-brain imaging of neuronal activity in zebrafish larvae^{24,25}. Through a series of technical implementations, comprising fine adjustment of excitation light polarisation²⁶, use of two coplanar counterpropagating light-sheets for spatially-alternating illumination, avoidance of any bulky mechanical moving components to perform the volumetric acquisition, and concentration of the fluorescence light on the detector sensor, we optimized the setup for maximum SNR, thus achieving high-speed volumetric imaging using non-linear excitation. We applied the system to investigate the neuronal dynamics occurring in the larval zebrafish brain during epileptic seizures. Indeed, we mapped in real-time, on a brain-wide scale and with cellular resolution, the onset and propagation of acute seizures, as induced by the convulsant drug pentylenetetrazol (PTZ), at the same time avoiding detrimental photostimulation on a highly susceptible system such as an epileptic brain. In this work, we show that the presented 2P LSFM design enables high spatio-temporal resolution while avoiding visual stimuli, thus allowing unprecedented access to whole zebrafish brain epileptic dynamics and observing for the first time the emergence of caudo-rostral ictal waves (CRIWs).

Methods

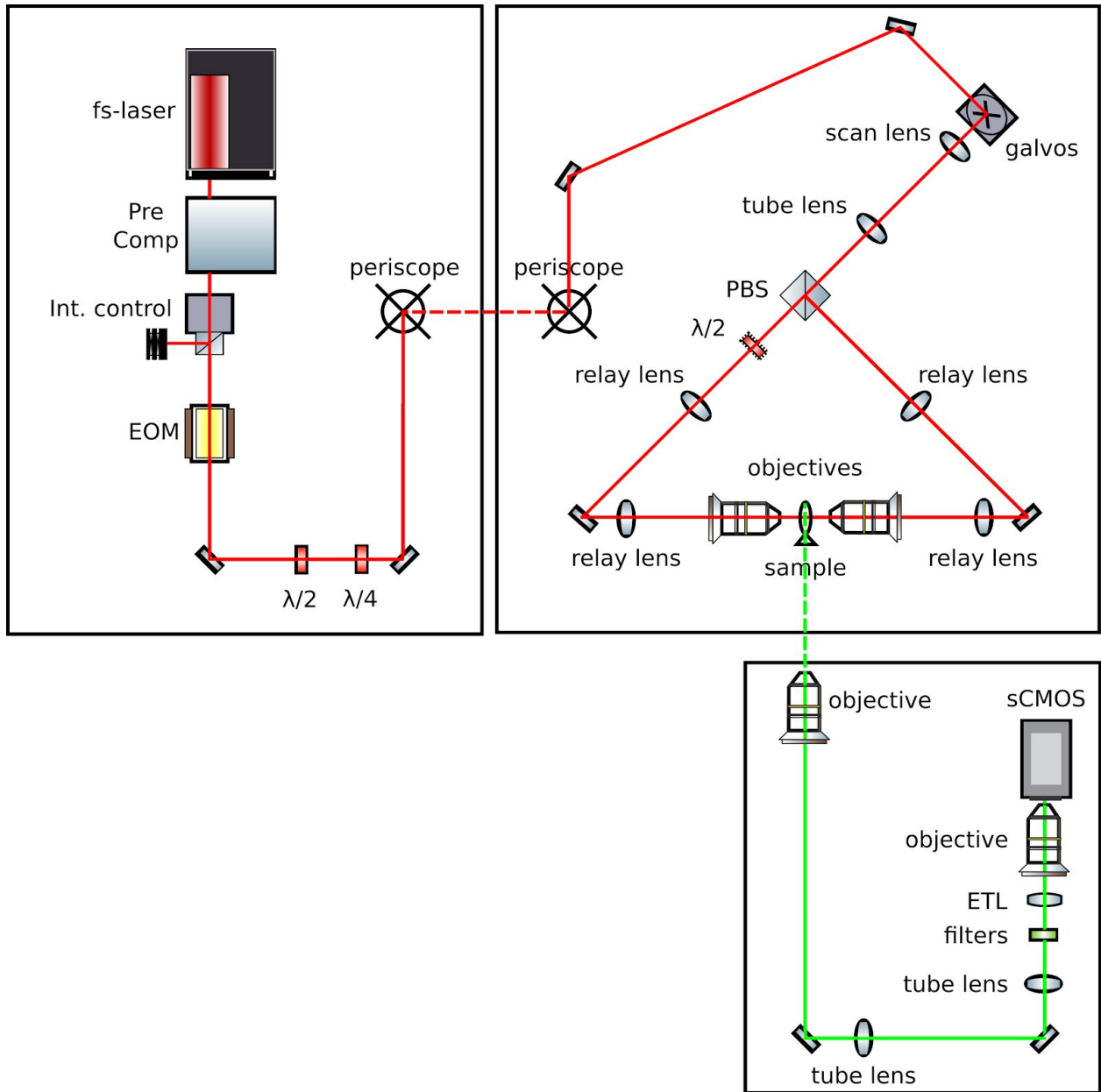


Fig. 1. Schematic of the employed custom-made 2P LSFM setup. fs-laser: femtosecond laser. Pre Comp: group delay dispersion precompensation unit. Int. control: power intensity control unit. EOM: electro-optic modulator. $\lambda/2$: half-wave plate. $\lambda/4$: quarter-wave plate. galvos: hybrid galvanometric mirrors assembly. PBS: polarising beam splitter. ETL: electrically tunable lens. Red lines: excitation beampath, green lines: detection beampath. Dashed segments indicate vertical paths.

2P LSFM setup

The employed 2P LSFM setup is depicted in Fig. 1. A tunable Ti-Sa pulsed laser (Chameleon Ultra II, Coherent) is used to generate the excitation light at 930 nm. The laser is coupled with a pulse compressor unit (PreComp, Coherent) to pre-compensate for the group delay dispersion. At the exit of the pulse compressor, the laser beam is attenuated using a half-wave plate and a Glan-Thompson polariser that dumps part of the beam.

The beam then passes through an electro-optical modulator (EOM, 84502050006, Qioptiq) that switches the polarisation state of the light between two orthogonal states with a frequency of 100 KHz. After the EOM, a quarter-wave plate is used to pre-compensate for the polarisation distortions and a half-wave plate is employed to rotate the couple of light polarisation planes in order to be parallel or perpendicular with respect to the optical table surface.

The light is then routed to an hybrid pair of galvanometric mirrors by a periscope and a pair of steering mirrors. One of the galvanometric mirrors is a fast resonant mirror (CRS-8 kHz, Cambridge Technology) and it is used to scan the beam along the fronto-caudal direction of the larva with a frequency of 8 KHz to digitally generate the light sheet. The other galvanometric mirror is a closed-loop mirror (6215H, Cambridge Technology) and it is used to scan the light-sheet along the dorso-ventral direction of the larva with a frequency of 5 Hz.

Two excitation dry objectives are placed at the lateral sides of the larva, outside the sample chamber. The scanned beam is routed to one of the two excitation objectives (XLFLUOR4X/340/0,28, Olympus) by means of a scan lens (50 mm focal length), a tube lens (75 mm focal length) and a pair of relay lenses (250 mm and 200 mm focal

lengths). The lens series after the galvos magnifies the beam diameter 1.2 times, therefore the objective pupils are underfilled. When the incoming light is polarised perpendicularly to the table surface by the EOM, it is diverted by a polarising beam splitter placed between the tube lens and the first relay lens to illuminate the second excitation arm. Immediately after this beam splitter, a half-wave plate is used to rotate the light polarisation plane so that the light from both the excitation objectives is polarised parallel to the table surface. Finally, a pair of relay lenses identical to the one on the first excitation arm is used to route the beam to the second excitation objective.

The excitation light is focused inside the fish-water-filled custom-made sample chamber. This chamber is walled by thin (0.17 mm) glass surfaces and is open on the top. It is thermostated using a dedicated custom-made closed-loop controller.

The chamber is designed to hold a custom-made glass slide. The glass slide is modified to have a raised glass wedge at the center, on the top of which the larva is placed. In this way the focused light beams are not distorted by the presence of the adjacent glass slide surface.

The fine three-dimensional placement of the sample under the detection objective is performed by moving the sample chamber with three micro-positioning stages (M-521.DD1, M-511.DD1 and M-501.1DG, Physik Instrumente) while observing the detection-objective relative position with an IR-sensible auxiliary camera (UI-1240SE-NIR-GL, iDS) placed frontally to the larva, outside the chamber.

A water-immersion high-numerical aperture (NA) detection objective (XLUMPLFLN20XW, Olympus, NA=1) placed on the dorsal side of the larva is used to collect fluorescence emission. For this objective we use a tube lens with a focal

length of 300 mm. The collected light is then routed to the sCMOS camera (ORCA-Flash4.0 V3, Hamamatsu) by a relay system composed by an additional tube lens (focal lens: 200 mm) and a dry objective (UPLFLN10X2, Olympus, NA=0.3). The total magnification of the detection arm is 3×.

Immediately before the camera objective pupil we placed the filter wheel and an electrically-tunable lens (ETL). The ETL (EL-16-40-TC-VIS-5D-C, Optotune) is used to remotely scan the focal plane of the sample-side detection objective in synchrony with the light sheet motion. To select GCaMP6s emission we used a green fluorescence filter (FF01-510/84-25 nm BrightLine® single-band bandpass filter, Semrock) placed in the filter wheel.

The two excitation objectives and the sample-side detection objective are mounted on objective scanners (PIFOC P-725.4CD, Physik Instrumente). Before each acquisition the axial positions of the objectives are tuned in order to overlap the scanning range of the ETL with that of the closed-loop galvanometric mirror and to homogeneously illuminate the sample from the sides.

Acquisition control

The custom-made microscope is controlled by two workstations (Precision Tower 5810 and Precision Tower 7810, Dell), one of which is dedicated exclusively to the camera control, exploiting a frame-grabber device and a RAID-0 array of four fast SSD devices, while the other one is used to manage all the other microscope hardware, also using a data acquisition device (PCIe-6353, National Instruments). All the imaging control processes are performed by custom-made software written in G-Code (LabVIEW, National Instruments).

PSF and beam diameter measurements

Detection point spread function (PSF) measurements were performed visualizing fluorescent beads with a diameter of 2.5 μm included in agar gel, employing a blue LED source for excitation. Excitation beam diameter measurements were performed by imaging the fluorescent emission induced in a concentrated fluorescein solution.

Laser power

For all the imaging sessions, the power of the excitation beam at the exit of the EOM was set between 0.9 W and 1.0 W. These values were chosen after performing preliminary studies about phototoxicity. In brief, we continuously imaged 10 larvae for extended periods of time (more than 1 hour) and with different excitation powers (between 0.6 W and 1.0 W). For each larva we reported the time when photodamage appeared in the brain volume as areas of sustained activation of the calcium sensor.

Exploiting the statistical programming language R²⁷ and the software package OpenBUGS²⁸, we then employed a Bayesian Weibull survival model with non-informative prior distributions to estimate the probability of observing photodamage as a function of imaging time. In particular, we computed that with an excitation power of 0.9 W there is an 80% probability not to observe photodamage when imaging continuously for 30 minutes, as shown in supplementary Fig. 1.

The cumulative power levels at the excitation objective pupils correspond to the ~40% of the power level at the exit of the EOM (~20% for each objective in time-average). Therefore, a power less than 0.4 W is directed toward the liquid-filled sample chamber from the two sides. No photodamage was observed during subsequent experimental imaging sessions.

Imaging sessions

Each imaging session started with a 5-minute control acquisition before the exposure to the convulsant. After the convulsant exposure, the imaging session proceeded alternating 5-minute acquisitions every 10 minutes for 6 cycles to reduce thermal accumulation¹⁹. Therefore, for each animal we imagined 30 minutes of aberrant neuronal activity during seizure onset and propagation spanning a total time of 60 minutes.

The volumetric imaging was performed at 5 Hz with 31 stacked z-planes spanning an axial size of 150 μm . A spacing of 5 μm along the axial dimension was chosen because it coincides with the value of the half width at half maximum of the detection axial PSF. The image pixel size is $\sim 2.2 \mu\text{m} \times 2.2 \mu\text{m}$ and we acquired 512×512 pixel images with 12 bit depth of integer grey levels. This pixel size is well suited to the transversal detection PSF size (6 μm FWHM), thus granting a sampling rate fulfilling the Nyquist criterion. The acquisition time for each image is 5.8 ms, while 20 ms were allocated for the ETL flyback time.

Zebrafish larvae

We observed a total of 12 zebrafish (*Danio rerio*) larvae aged 4 days post fertilization (dpf). The homozygous albino background²⁹ transgenic strain Tg(elavl3:H2B-GCaMP6s)^{15,30} employed expresses the fluorescent calcium sensor GCaMP6s under a pan-neuronal promoter with nuclear localization. Fish were maintained according to standard procedures³¹ and their handling was carried out in accordance with European and Italian law on animal experimentation (D.L. 4 March 2014, no. 26), under authorization no. 407/2015-PR from the Italian Ministry of Health.

Before the imaging sessions, the larvae underwent a mounting procedure as we previously described³². Briefly, each larva was paralyzed with a solution of d-tubocurarine (2 mM; 93750, Sigma-Aldrich) to avoid movement artefacts, included in 1.5% (w/v) low gelling temperature agarose (A9414, Sigma-Aldrich) in fish water (150 mg/L Instant Ocean, 6.9 mg/L NaH₂PO₄, 12.5 mg/L Na₂HPO₄, pH 7.2), then mounted on a custom-made glass support and immersed in fish water thermostated at 28.5 °C. After the initial 5-minute control acquisition, each larva was exposed to convulsant agent PTZ at one of the following final concentrations: 1, 2.5, 7.5 and 15 mM. We randomly assigned three larvae to each concentration. Stock solutions of PTZ were prepared by dissolving it in milliQ water, while the final concentrations used in the experiments were obtained by diluting each stock in fish water.

Post-processing

After the acquisitions, each time-lapse recording was manually inspected to identify movement artefacts. Where present, these artefacts were removed; in this way, from a single time-lapse movie, several motion artefact-free sub-movies were generated. The raw fluorescence images were then preprocessed as described in the following. First two volumetric masks were computed as the sets of pixels whose values were smaller than two arbitrarily-chosen threshold values. The mask computed on the larger threshold value was then subjected to a morphology opening operation. After that, the final mask was computed as the binary-set union between the two masks. The values of all the pixels identified by the final mask were set to zero. After the masking procedure, the 12-bit integer fluorescence images were converted in 32-bit floating point pixel-based $\Delta F/F_0$ signal using the following formula:

$$\Delta F/F_0 = \frac{F - F_0 - D}{F_0 - D},$$

where F_0 is computed as the pixel-based first decile value along the temporal dimension, while D is computed as the nearest lower integer of the lowest unmasked F_0 value.

Great care was taken to mount the larvae in the same position and orientation, nevertheless, in order to enhance the inter-sample consistency, we spatially aligned the brain volumes acquired from different animals in a post-processing passage. This alignment procedure was performed using a series of custom-made Python scripts that we made publicly available on GitHub (<https://github.com/lens-biophotonics/2P-LSFM-align>). First, time-lapse $\Delta F/F_0$ movies were spatially interpolated along the axial dimension to an almost isotropic voxel size of $2.2 \mu\text{m} \times 2.2 \mu\text{m} \times 2.0 \mu\text{m}$. Then an animal-specific rotation matrix was applied. Finally, the rotated stacks were binned to the final voxel size of $4.4 \mu\text{m} \times 4.4 \mu\text{m} \times 4.0 \mu\text{m}$. In the binning procedure only the unmasked voxels were taken into account, so that relevant border information was not degraded. In order to generate the rotation matrices, we time-averaged one stack for each animal and then we confronted the result with a reference stack. We exploited a simulated annealing algorithm to optimize the rotation parameters, using the numerosity of the intersection set between the unmasked voxels of the two stacks as fitness value. Finally, the parameters of each matrix were fine-tuned manually by visually exploring the rotation results. For the resulting overlaid stacks, we considered as unmasked only those pixels that were unmasked in the same position in all the original stacks.

Lag analysis

To perform lag analysis, we computed the temporal cross-correlation between each voxel-based calcium trace and the global encephalon average trace. The voxel-based lag value is defined as the temporal cross-correlation shift associated with the maximum value of the coefficient of determination. Cross-correlation between traces was computed using the Pearson's coefficient.

To generate single-trial voxel-based lag maps, we colour-mapped the lag value, limited to the unmasked voxels showing a statistically significant correlation. We generated aggregated voxel-based lag maps by colour-mapping the median values of the single-trial voxel-based lags, considering only the unmasked and statistically significant voxel of each acquisition.

For Region-Of-Interest (ROI)-based analysis, the lag value was computed for each acquisition as the median lag value among all the unmasked voxels in the ROIs that display also a statistically-significant correlation. If the percentage of voxels in the ROI displaying a statistically-significant correlation with respect to the total number of unmasked voxels was lower than 20%, then the observation was discarded.

ROI-based statistical analysis of lag delay was performed using Kruskal–Wallis one-way analysis of variance followed by post-hoc pairwise multiple comparison procedure with Dunn test. Multiplicity correction was carried out with the Benjamini-Hochberg procedure controlling the false discovery rate (FDR) at 5%.

Lag histograms for the relative frequencies of voxel-based lag values were computed for each acquisition and each ROI, and then aggregated plots were generated by computing the first, second and third quartiles of the distributions for each class of the plots.

Statistical analysis

Statistical analysis of the variation of the mean $\Delta F/F_0$ value over exposure time was carried out by performing a linear regression for each ROI and each PTZ concentration, exploiting the exposure time as the independent variable. As the dependent variable, we employed a single aggregated weighted average of the stack-based mean $\Delta F/F_0$ values (restricted to the unmasked voxels) for each time-point, employing the number of temporal frames as weight. Statistical significance was asserted if the p-value of the regression coefficient resulted lower than 0.05.

For the statistical treatment of all other ROI-based and voxel-based analyses, we employed general linear mixed models³³ (GLMMs) implemented in the R language in which we defined the animals as a random factor. The response variables used in ROI-based analyses were computed as the ROI-based means (restricted to the unmasked voxels) of the response variables studied in voxel-based analyses. For the analyses of data relating to submaximal PTZ concentrations, we set the categorical PTZ concentrations and the interaction between the categorical PTZ concentrations and the exposure time as fixed factors in the GLMMs. For the analyses of data relating to maximal PTZ concentration, we instead set only the categorical PTZ concentrations as a fixed factor. Correlation coefficients were computed employing the Pearson product-moment correlation coefficient formula. For the voxel-based analyses, we used the frequentist package lmerTest³⁴ and then we corrected for the multiplicity using the Benjamini-Hochberg procedure, controlling the false discovery rate (FDR) at 10% to test statistical significance. For voxel-based analyses of data relating to submaximal PTZ concentration, we extracted the

p-values directly from the GLMMs, while for the analyses of data relating to maximal PTZ concentration we employed linear contrasts based on the respective GLMM. For the ROI-based analyses we used the Bayesian package brms³⁵ employing NUTS sampler and setting uninformative priors. For the analyses of the correlation coefficients and of the mean $\Delta F/F_0$ values at submaximal PTZ concentration, statistical significance was tested by computing the credibility intervals (CIs) at 95% for the posterior distributions of parameters. For the analysis of the correlation coefficient at maximal PTZ concentration, statistical significance was tested employing Bayesian non-linear hypothesis testing based on the respective GLMM and setting the statistical significance threshold at 95% for the posterior probabilities.

Results

In 2P LSFM the main constraint on volumetric acquisition frequency is represented by the SNR. Therefore, the system we devised (shown in Fig. 1) was specifically designed to maximize this parameter. In particular, a quarter-wave retarder and two half-wave retarders are employed to carefully orient the polarisation plane of linearly-polarised excitation light, allowing to drastically increase the signal levels in 2P LSFM, as we showed in a previous article²⁶. This effect is achieved by photoselecting a subpopulation of fluorophores that will emit fluorescence light preferentially toward the detection objective, thus increasing the collection of light. Due to the existence of optical constraints that bind the longitudinal and the transversal dimensions of a (2P) light-sheet (i.e. the confocal parameter), we opted to use double-sided illumination, thus exploiting two partially-overlapped thinner and shorter light-sheets in place of a single, thicker, and longer one. In this way, the

radial dimension of the light-sheets ($\sim 7.5 \mu\text{m}$ FWHM) can be matched with the axial detection PSF size ($\sim 10 \mu\text{m}$ FWHM), thus achieving a better axial resolution while at the same time illuminating the whole sample plane. Moreover, due to the two counterpropagating beams, this excitation geometry provides also a very homogeneous sample illumination and a strong attenuation of striping artefacts³⁶, with these effects being even more prominent due to the reduced scattering of the excitation light granted by the IR wavelength. It should be noted, finally, that the radial dimension of the light sheets was chosen also to match the typical dimension of the zebrafish neuron cell bodies ($\sim 5 \mu\text{m}$), thus potentially maximizing the signal generation from the nuclear-localized fluorophores.

In 2P fluorescence, the light emission is proportional to the square of the excitation light intensity. For this reason it is important to maximize the excitation peak power. Therefore, the beam splitter that we used to generate the two excitation beams was chosen to be polarising. In this way the two halves of the field-of-view are alternatively illuminated depending on the EOM operation state (and, therefore, on the instantaneous light-polarisation state). The OEM operating frequency is three orders of magnitude larger than the camera acquisition frequency, therefore no blinking can be observed in the recordings. This arrangement allows to double the fluorescent signal compared to using a non-polarising beam splitter because the peak power levels are preserved, albeit the illumination time is halved. In fact, a non polarising beam splitter would halve the peak power, inducing a quadric decrement in the signal that would not be compensated by the preservation of the total illumination time (that linearly affects the signal levels).

In order to collect as much fluorescence light as possible, it is important to use a high-NA detection objective and therefore to resort to an immersion one, avoiding dry objectives. On the other hand, if an immersion objective is scanned along the axial dimension to synchronize the position of the detection focal plane with the position of the illumination light-sheet, then pressure waves impinging on the sample are generated during high-speed volumetric acquisitions (> 2 Hz), thus disrupting the imaging. For this reason, we decided to remotely scan the focal plane using an ETL, while keeping the objective still. We installed the ETL in our setup employing a configuration similar to the one described by Fahrbach and collaborators³⁷. This configuration introduces a small degradation of optical telecentricity, i.e. an axial-position dependent magnification component. The magnification alteration at the two extremes of the range commonly used in our acquisitions ($150\text{ }\mu\text{m}$) was quantified and it was found to be below 7% with respect to the magnification at the center of the range (a level similar to what described by Fahrbach and collaborators³⁷). Therefore, considering the functional (i.e. not structural) scope of our observations, this effect is deemed negligible.

The image generated by the detection objective tube lens is projected to the camera sensor by an optical relay system (composed by a second couple of objective and tube lens) that also demagnifies it. In this way, the final magnification of the detection arm is $3\times$, i.e. radically different from the original magnification of the sample-side objective ($20\times$). This enlargement of the field-of-view comes at the expense of optical aberrations in the field periphery, however these aberrations are still acceptable in the area occupied by the sample, especially considering the functional nature of our observations. On the other hand, in this way we are able to take advantage of the

light collection capability of a high-NA objective while benefiting from the large field-of-view. In order to achieve these results, care was taken to match the NA of the sample-side objective (NA_s) with that (NA_c) of the camera-side objective ($NA_s \cdot M \approx NA_c$, where M is the lateral magnification). This demagnification also offers the advantage to focus the image to a small central portion (512×512 pixels) of the sCMOS camera sensor providing a double benefit: an enhanced number of photons collected by each camera pixel and an increased image readout frequency. The image pixel size ($2.2 \mu\text{m}$) was ultimately accurately chosen in order to sample neuronal cell bodies ($\sim 5 \mu\text{m}$) according to the Nyquist principle.

A further optimization to increase the SNR is the use of a pulse compressor to precompensate for the group delay dispersion induced by the optics and, above all, by the long path travelled by the focussed light after the excitation objectives inside the water-filled imaging chamber.

Finally, the use of a resonant galvanometric mirror to generate the digitally-scanned light-sheed guarantees a sufficient lateral scan speed (8 KHz).

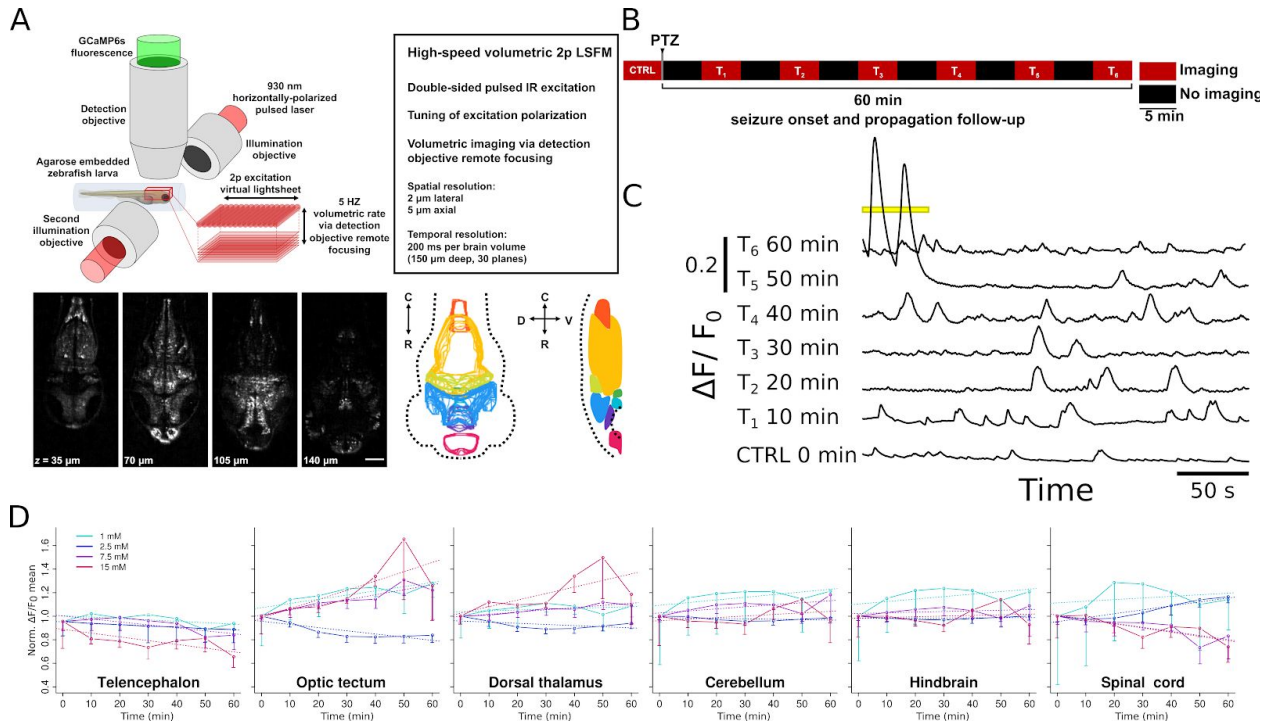


Fig. 2. A. Top-left: close-up schematic showing the axial scanning direction and the geometric disposition of the larva and of the excitation and detection objectives. Top-right: summary of the setup performances. Bottom-left: four z-planes showing temporal maximum intensity projections at different dorso-ventral depths of a larva (indicated on the panels, with respect to the dorsal surface). Scale bar: 100 μm . Bottom-right: outlines of the different ROIs (in different colours) considered in the analysis; left: transversal projection, right: longitudinal section over larval midline. **B.** Schematic diagram of the temporal protocol followed during the experimental sessions, alternating imaging and non-imaging periods after the control acquisition followed by PTZ exposure. **C.** Examples of $\Delta F/F_0$ traces from a single larva exposed to 15 mM PTZ, recorded during the different acquisition phases described in panel B. Traces were generated by averaging the activity signal over the whole brain. The yellow bar indicates an individual ictal event that happened 50 minutes after PTZ exposure. **D.** Line plots of the mean values of the $\Delta F/F_0$ traces as a function of the PTZ exposure time. Different colours indicate different PTZ concentrations, as indicated in the legend. The traces were generated by averaging the activity signal over different ROIs, as indicated on the plots. Linear fits for each PTZ concentration are indicated as dotted lines with corresponding colours. Half error bars indicate the standard error of the aggregated means. A small amount of jitter was applied on the error bars to improve visualization. All

the values were normalized on the mean $\Delta F/F_0$ value of the corresponding control acquisition at time zero.

The described 2P LSFM setup (Fig. 1) allowed us to visualize neurons in the intact larval zebrafish brain at cellular resolution (Fig. 2A, lower left panel), capturing neuronal activity in the entire brain every 200 ms. We applied 2P light-sheet functional imaging to monitor seizures induced by PTZ, a GABA_A receptor antagonist widely used as a convulsant drug^{38–40}, in 4 dpf larvae expressing the calcium indicator GCaMP6s^{15,30} in all neuronal nuclei. The whole-brain access guaranteed by the system allowed for fine monitoring of seizure onset and propagation across multiple anatomic districts spanning the entire brain. Indeed, we divided the encephalon in eight distinct anatomical regions: telencephalon, dorsal thalamus, optic tectum, medial tegmentum, interpeduncular nucleus (IPN), cerebellum and hindbrain, with the addition of the spinal cord; identified using available zebrafish brain atlases^{41,42} (Fig. 2A, lower right panel).

After an initial baseline recording, larvae were treated with PTZ at chosen concentrations (1, 2.5, 7.5 and 15 mM) and seizures dynamics were evaluated over one hour. We adopted a recording scheme consisting of five minutes of whole-brain recording interspersed with five minutes of rest (Fig. 2B), to avoid any possible photodamage induced in zebrafish larvae by continuous exposure to the incoming pulsed laser¹⁹.

Figure 2C shows typical whole-brain $\Delta F/F_0$ traces, observed at the different imaging time-points, of a zebrafish larva exposed to the maximal concentration of PTZ. After an initial increase in amplitude and frequency of global brain activity, between 10 and

40 minutes upon the addition of the convulsant drug, the scenario abruptly changes with the appearance of typical high-amplitude and low frequency ictal events (yellow highlight at T5, 50 min).

We thus investigated to which extent the tested PTZ concentrations affect neuronal activity over exposure time in the brain regions highlighted in Fig. 1A (shown in Fig. 2D). Indeed, while at the lowest dose (1 mM) PTZ induced a significant increase in neuronal activity over exposure time only in the optic tectum, testing the 2.5 mM concentration produced a significant rise of the activity over time only in the spinal cord, though inducing a decrease in both the optic tectum and the telencephalon. Finally, the two higher concentrations that were tested (7.5 mM and 15 mM) produced a significant increase of neuronal activity over time in the optic tectum (and also in the dorsal thalamus, only for the 7.5 mM concentration) while inducing a significant decrease in the spinal cord and in the telencephalon.

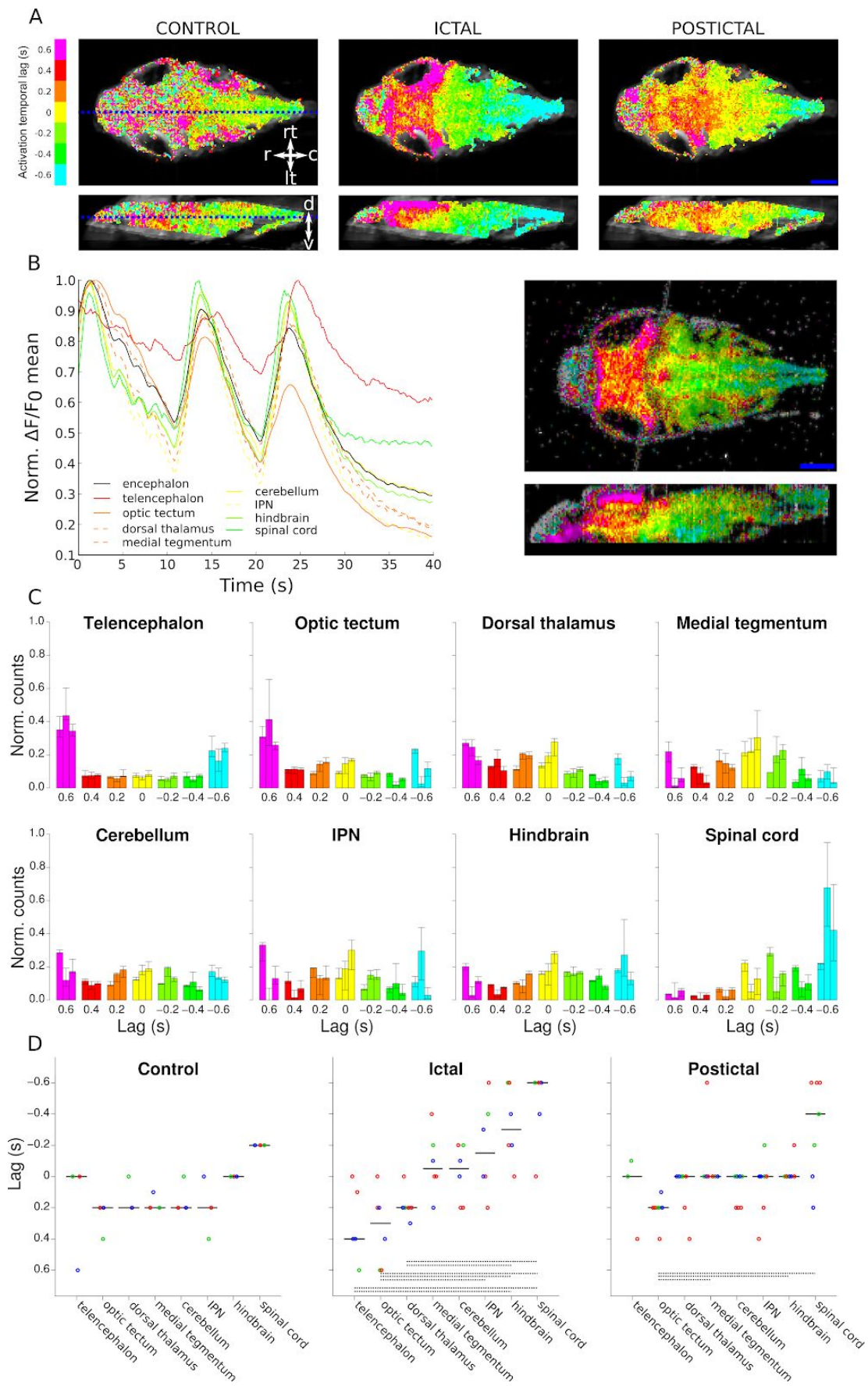


Fig. 3 A. Lag maps showing the voxel-based temporal position of the maximum of the cross-correlation function (coefficient of determination) between the voxel-based calcium signal and the global cerebral average during the control, the ictal and the postictal phases. These lag maps represent the aggregate results from all the larvae exposed to the maximal PTZ concentration. The lag value is colour-coded as specified by the colour map on the left. Masked or non-statistically significant voxels are depicted in grey values. Top row: transversal sections; bottom row: longitudinal sections. The sectioning planes are indicated as dashed blue lines on the first panels. Scale bar: 100 μm . **B.** Lag analysis for a single trial acquired during the ictal phase. Left: $\Delta F/F_0$ signal from different ROIs (indicated by different colours or different line types). The signals were normalized by dividing them for the respective maximum values. Right: single-trial lag maps. Top: transversal section; bottom: longitudinal section. Colour code, grey values and scale bar as in A. These images were generated in the hue, saturation, brightness colour-space and, differently from A, the voxel brightness is a function of its time-averaged calcium signal intensity. **C.** Histograms of the relative frequencies of the voxel-based lag values for each ROI (as indicated in the plots). The bar colours correspond to the colour code in A. The height of each bar corresponds to the median value of the single-acquisition-based frequency distribution, while the error bars indicate the first and the third quartiles of the distribution. The first, second and third bars in each lag class correspond to the control, ictal and postictal situations, respectively. **D.** Scatter plots of the median lag values for each condition (as indicated in the plots) and ROI (on the x-axis). Different colours indicate different larvae. Each point corresponds to a single acquisition. A small amount of jitter was applied on the x-axis to improve readability. Horizontal short bars indicate the median value for each ROI. Statistically significant differences are indicated by horizontal dotted lines on the bottom of the graphs.

We manually inspected the calcium traces computed as global cerebral average to find ictal activity⁴³. We observed ictal (and therefore also postictal) activity only in larvae that were exposed to the maximal concentration of PTZ (15 mM), as shown in Fig. 2C.

In these larvae we decided to study the spatio-temporal pattern of seizure spreading by computing the cross-correlation between the voxel-based and the global average activities. This procedure is justified by the fact that epileptic activity is by definition characterized by hyper-synchronicity, therefore performing the global cerebral mean makes the pathological features stand out by averaging out asynchronous activity. In this way, by identifying the voxel-based maxima in the temporal cross-correlation function (i.e. the “lag value”), it is possible to visualize the spatial spreading path of the seizure activity. We show the aggregate results from all the animals that were exposed to the maximal PTZ concentration in Fig. 3A. These maps clearly illustrate that during an ictal phase the pathological activity first emerges in the most caudal regions, such as the spinal cord, then gradually moves toward more rostral regions such as the optic tectum and the telencephalon. This caudo-rostral propagation pattern is not visible in the control condition (before PTZ exposure). On the contrary, in the postictal condition a similar pattern is observed, albeit less defined and less pronounced, thus further confirming the validity of our findings.

To assess the representativeness of the aggregated colour map of the ictal phase, we verified the concordance of the voxel-based lag-values of this map with those of the 9 recorded ictal events (deriving from the 3 exposed larvae) from which the aggregated map is derived. The results are shown in supplementary Fig. 2 and confirm the across-event consistency of the observed caudo-rostral pattern.

Moreover, this pattern does not emerge merely as an aggregate average, on the contrary, it is visible also in single-trial data, as we show in Fig. 3B.

In order to further characterize the observed lag-value behaviour, we computed voxel-based distributions of the lag values for each ROI and we show them in Fig.

3C. From these histograms it is evident that the lag values are distributed differently among the control, ictal and postictal conditions. Moreover, the shape of these distributions indicate that the median voxel-based lag values used to generate the maps shown in Fig. 3A are faithful indicators of central tendency for the lag distributions. In other words, since these distributions are not dominated by the most extreme upper and lower values, we can confirm that the observed caudo-rostral pattern emerges from a real, and correctly sampled, spatio-temporal development of neural activity.

Finally, in order to assess the differences between ROI-based lag values, we draw the scatter plots shown in Fig. 3D for the control, ictal and postictal conditions. We ordered the different ROIs on the x-axis based on the approximate position along the animal rostro-caudal axis. In this way a rostro-caudal order in the progression of the ROI-based lag values emerges clearly for the ictal condition. The statistical analysis confirmed the existence of significant differences among several rostral and caudal ROIs (p-value for Kruskal-Wallis test = 0.0002, q-value for post-hoc Dunn test < 0.05 for telencephalon versus hindbrain and spinal cord ROIs, for optic tectum versus IPN, hindbrain and spinal cord ROIs and for dorsal thalamus versus hindbrain and spinal cord ROIs), as shown at the bottom of the plots. Few of these differences are also observed in the postictal condition (p-value for Kruskal-Wallis test = 0.003, q-value for post-hoc Dunn test < 0.05 for optic tectum versus medial tegmentum, hindbrain and spinal cord ROIs), while no significant differences are observed in the control condition.

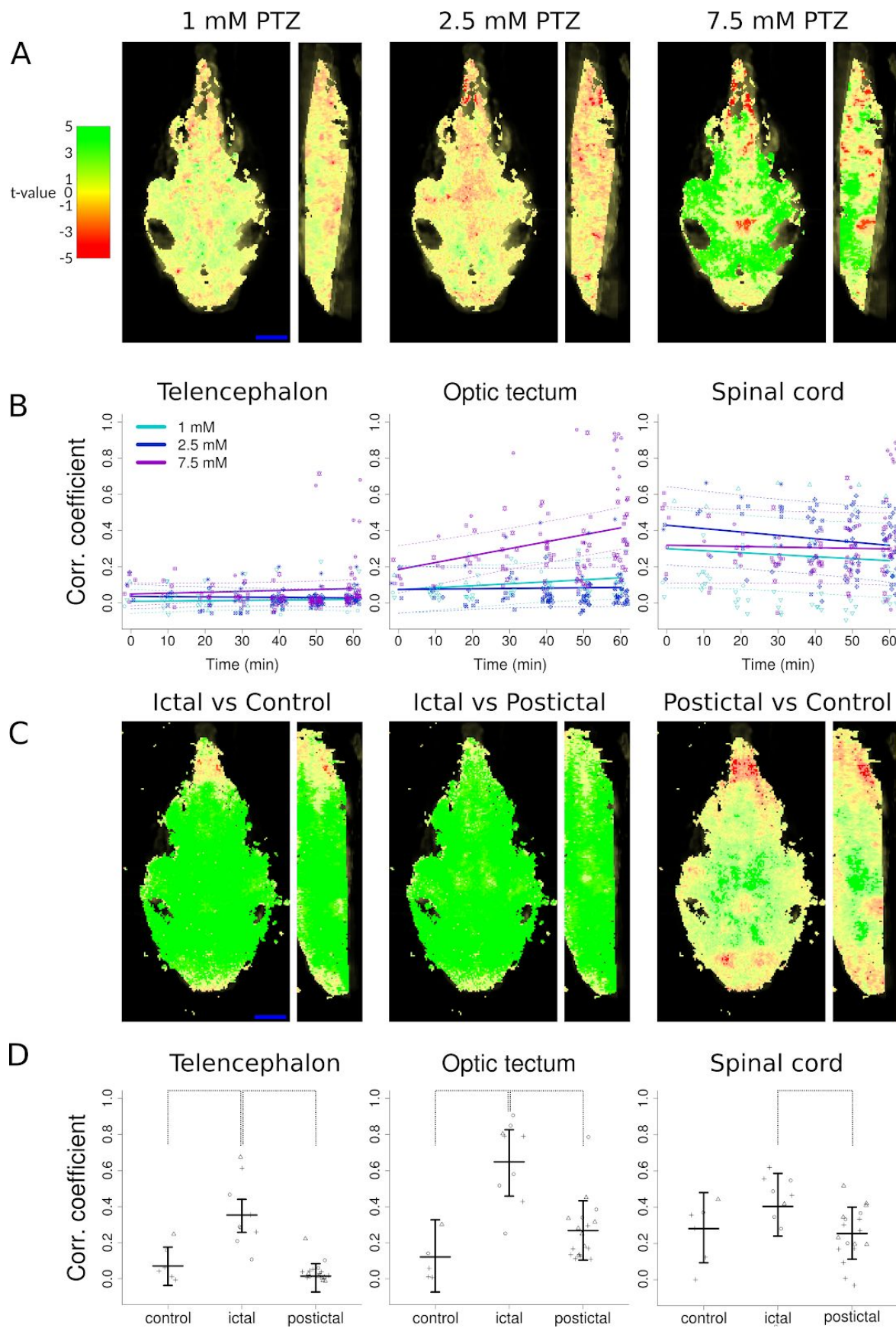


Fig. 4. A. Colour maps (longitudinal and transversal sections) depicting the effects of PTZ concentration and exposure time on the correlation coefficient value computed between single-voxel calcium activity and global calcium activity. These maps represent the aggregate results from all the larvae exposed to sub-maximal PTZ concentrations. Masked voxels are depicted in grey values, non-statistically significant voxels in unsaturated colours and statistically significant voxels in saturated colours. The voxel-based t-value associated to the effect of the interaction between PTZ concentration and exposure time is colour-mapped as described by the colour-bar on the left. Scale bar: 100 μ m. **B.** Scatter plots showing the distribution of the ROI-based (as indicated on the top) correlation coefficients (on the y-axis) as a function of PTZ concentration (different colours) and exposure time (on the x-axis). Data related to different animals are indicated by different shapes. A small amount of jitter was applied on the x-axis to increase readability. Solid lines indicate predicted values generated by the Bayesian model, while dotted lines indicate the 95%-CIs. **C.** Colour maps (longitudinal and transversal sections) depicting the effects of the control, ictal and postictal conditions on the correlation coefficient value. These maps represent the aggregate results from all the larvae exposed to maximal PTZ concentration. The colours map voxel-based t-values associated to the effect of the condition. Colour code, colour saturation, grey values and scale bar as in A. **D.** Scatter plots showing the distribution of the ROI-based (as indicated on the top) correlation coefficients (on the y-axis) at maximal PTZ concentration in control, ictal and postictal conditions (on the x-axis). Data related to different animals are indicated by different shapes. A small amount of jitter was applied to the x-axis to increase readability. The horizontal lines indicate predicted values generated by the Bayesian model and their error bars indicate the 95%-CIs. Statistically significant differences are indicated by dotted lines.

In order to characterize how the degree of hyper-synchronicity varies during the development of seizure activity, we studied the trend of the correlation coefficient between the voxel-based calcium traces and the global average calcium trace. We observed that some of the ROIs exhibit similar neuronal behaviours, therefore here

we mainly focussed on three ROIs: telencephalon, optic tectum and spinal cord, that summarize the globality of the observed neuronal behaviours. Aggregate results from all the larvae are shown in Fig.4. We analyzed the data from animals exposed to maximal and submaximal concentrations of PTZ separately, since we have shown that only the former are characterized by the emergence of ictal activity.

For submaximal concentrations, we characterized the temporal dependence of the correlation coefficient values on the exposure time and we generated colour maps based on this effect, quantified as t-value, while checking its statistical significance.

As shown in Fig.4A, almost no statistically significant effects are observed for 1 mM PTZ concentration, while for 2.5 mM PTZ concentration we observed a significant negative correlation for few voxels, mostly located in the spinal cord in addition to a small number of others dispersed (but not isolated) throughout the encephalon.

Conversely, for 7.5 mM PTZ concentration we observed the emergence of a widespread positive correlation between the voxel-based calcium traces and the global average trace, meaning that the value of the correlation coefficient increases with the exposure time. The increased correlation among neuronal activity is the hallmark of seizures, even when ictal activity is not yet present. It is interesting to note that some subregions show an unexpected appearance of negative correlation, such as part of the spinal cord and the medial tegmentum, meaning that for these subregions the value of the correlation coefficient actually decreases with the increasing of the exposure time.

We then performed the same analysis at ROI level and no statistically significant effect was visible for 1 mM and 2.5 mM PTZ concentrations, as shown in Fig. 4B. On the contrary, for the 7.5 mM PTZ concentration, the correlation coefficient increases

during exposure time for ROIs such as the optic tectum, the hindbrain, the cerebellum and the dorsal thalamus in a statistically significant manner (the 95%-CI excludes the zero value). The decrease observed for the spinal cord ROI, however, did not result as significant; this lack of significance can be explained by the fact that the decrease in the correlation coefficient detected for small subregions included in this ROI is washed out when taking into account the whole region.

We also studied the correlation value differences among ictal, postictal and control conditions in animals exposed to the maximal concentration of PTZ (15 mM) and the aggregate results (for all the exposed animals) for the voxel-based analyses are shown in Fig. 4C. We observed a significant and widespread increase in the correlation coefficient in the ictal condition when compared to control or postictal conditions for the whole encephalon. On the contrary, we observed a reduced number of voxels showing significant differences between the postictal and control conditions in the encephalon, the majority of them exhibiting an increase in the correlation coefficient and being concentrated in subregions belonging to the inner parts of midbrain and hindbrain. Interestingly, the spinal cord behaves differently, showing almost no differences between ictal and control conditions, while a significant decrease in the correlation coefficient can be observed in its most dorsal subregion in the postictal condition compared to the control condition. Finally, in the comparison between the ictal and the postictal conditions, the spinal cord behaves similarly to the encephalon, showing a widespread increase in the correlation coefficient.

We characterized these differences at ROI level and the results are shown in Fig. 4D. We observed an increase in the correlation coefficient for the ictal condition

compared to the control or the postictal conditions for all the ROIs belonging to the encephalon, e.g. both for the telencephalon (+0.28 increase, 90%-CI: +0.18, +0.38, posterior probability \sim 100% and +0.34 increase, 90%-CI: +0.26, +0.42, posterior probability \sim 100%, respectively) and the optic tectum (+0.53 increase, 90%-CI: +0.36, +0.70, posterior probability \sim 100% and +0.38 increase, 90%-CI: +0.25, +0.51, posterior probability \sim 100%, respectively) ROIs. Conversely, in the comparison between the postictal and the control conditions we observed only a single significant difference in the correlation coefficient among the ROIs belonging to the encephalon: an increase for the dorsal thalamus ROI (+0.14 increase, 90%-CI: +0.03, +0.26, posterior probability = 98%). Remarkably, we did not observe significant differences for the spinal cord ROI comparing the ictal or the postictal conditions to the control condition, while we observed a significant increment (+0.15 increment, 90%-CI: +0.02, +0.29, posterior probability = 97%) in the correlation coefficient for the ictal condition compared with the postictal condition.

Discussion and conclusions

We developed a novel 2P LSFM setup employing pulsed IR excitation light to perform high-speed cellular-resolution imaging of the larval zebrafish brain.

Compared to conventional 1P LSFM (employing excitation in the visible range), 2P LSFM, owing to low 2P absorption probability, is prone to low SNR issues, especially when performing rapid volumetric imaging. Hence, we adopted a series of technical implementations to optimize the setup for maximum SNR. Particularly, we alternated the illumination of the two halves of the field-of-view to maximize the peak power of

excitation light, we controlled the excitation light polarisation to orient the emission toward the detection objective²⁶, we employed a remote focussing approach to enable signal collection by a high-numerical aperture immersion objective (without generating pressure waves on the sample), and finally we optically demagnified the image on the detector sensor to decrease readout and integration times. Collectively, the implementations adopted enabled for the first time fast volumetric imaging using non-linear excitation.

We demonstrated the importance of employing high-speed non-visible excitation LSFM to map the spatio-temporal onset and propagation of epileptic seizures induced by the convulsant drug PTZ in the zebrafish brain. Indeed, in recent years two research groups exploited the optical sectioning abilities of LSFM, though using visible excitation, to study neuronal dynamics underlying seizures in zebrafish larvae. Particularly, Winter and colleagues⁴⁴ first applied LSFM to the study of seizures, mapping a large part of the larval encephalon, without however achieving single-cell resolution and reaching a volumetric temporal resolution (0.5 Hz) sufficient to detect slow fluorescence trends but not rapid Ca^{2+} dynamics. Rosch and collaborators⁴⁵ achieved 20 Hz seizures mapping, yet on a single plane of the larval brain, thus failing to attain a comprehensive overview of whole-organ dynamics.

Using our novel system, we found that larval brain regions are differently recruited during seizures. Interestingly, some regions of the encephalon show an unexpected concentration-dependent dichotomic effect of PTZ on zebrafish functional connectivity. In particular, at a lower tested concentration (2.5 mM) the convulsant

drug induces a slight but significant reduction in neuronal activity in brain regions such as the telencephalon and the optic tectum, compared to pre-exposure levels (Fig. 2D). This scenario dramatically changes at the highest tested concentrations. In fact, when exposed to 7.5 mM PTZ, the larval brain shows significantly increased activity and synchronicity in regions such as the optic tectum and the dorsal thalamus (Figs. 2D and 4A). In addition, a similar effect is observed also for the spinal cord, that often displayed remarkably opposed dynamics with respect to encephalic regions. Indeed, the neural activity in the spinal cord showed an increase when exposed to a lower PTZ concentration (2.5 mM) and a decrease when exposed to the highest concentrations (Fig. 2D).

Moreover, when exposed to saturating PTZ concentration (15 mM), zebrafish larvae undergo a profound functional connectivity rearrangement, marked by an overall increase in neuronal activity synchronicity (Fig. 4C), which eventually brings to the appearance of ictal-like events, i.e. paroxysmal activity typical of acute seizures. During this phase we observed and described for the first time, to the best of our knowledge, CRIWs: rhythmic ictal waves propagating in caudo-rostral direction (Figs. 2C and 3). CRIWs are characterized by high-amplitude calcium transients, which are realistically generated by thousands of closely paced action potentials. Indeed, in this scenario, where all the inhibitory GABAergic synapses are dimmed by high PTZ concentrations, excitatory drive is predominant. Firing of neurons, whose activity is usually curbed by the inhibitory tone, may trigger other neuronal populations to fire, generating an avalanche effect which determines the seizure propagation we

observed. CRIWs are then followed by postictal activity, a state characterized by a marked overall depression of neuronal activity. Particularly, in the postictal phase we observed a decreasing synchronicity trend affecting subregions included in the telencephalon, in the medial tegmentum and in the spinal cord (Fig. 4C), likely underlying the ataxic phase observed during postictal behaviour³⁸.

Interestingly, despite the entire ictal wave typically lasts a few seconds, it consistently spans the entire brain, from the most caudal regions to the most rostral ones, in about 1 second, a time-frame inaccessible to previous 2P light-sheet setups, unable to reach such a high acquisition frequency^{23,46}. Compared to post-processing interpolation methods, which could be used to upscale the temporal resolution in the calculation of lag values based on non-trivial inferences on in-vivo non-linear dynamics of the calcium sensor, our native 5 Hz whole-brain sampling frequency will allow future experiments involving for example real-time optogenetic suppression of ongoing seizure activity based on closed-loop feedback approaches.

The system we devised, employing non-visible excitation and reaching high volumetric sampling frequency, allows the spatio-temporal description of CRIWs, taking a step forward in the description of whole-brain dynamics and functional connectivity reorganization during pharmacologically-induced acute seizures in zebrafish larvae.

This technique, proved successful in a delicate model such as an unstable epileptic brain, might be applied in the future also to other experimental models in which unwanted visual stimulation could be detrimental to unveil the neural dynamics

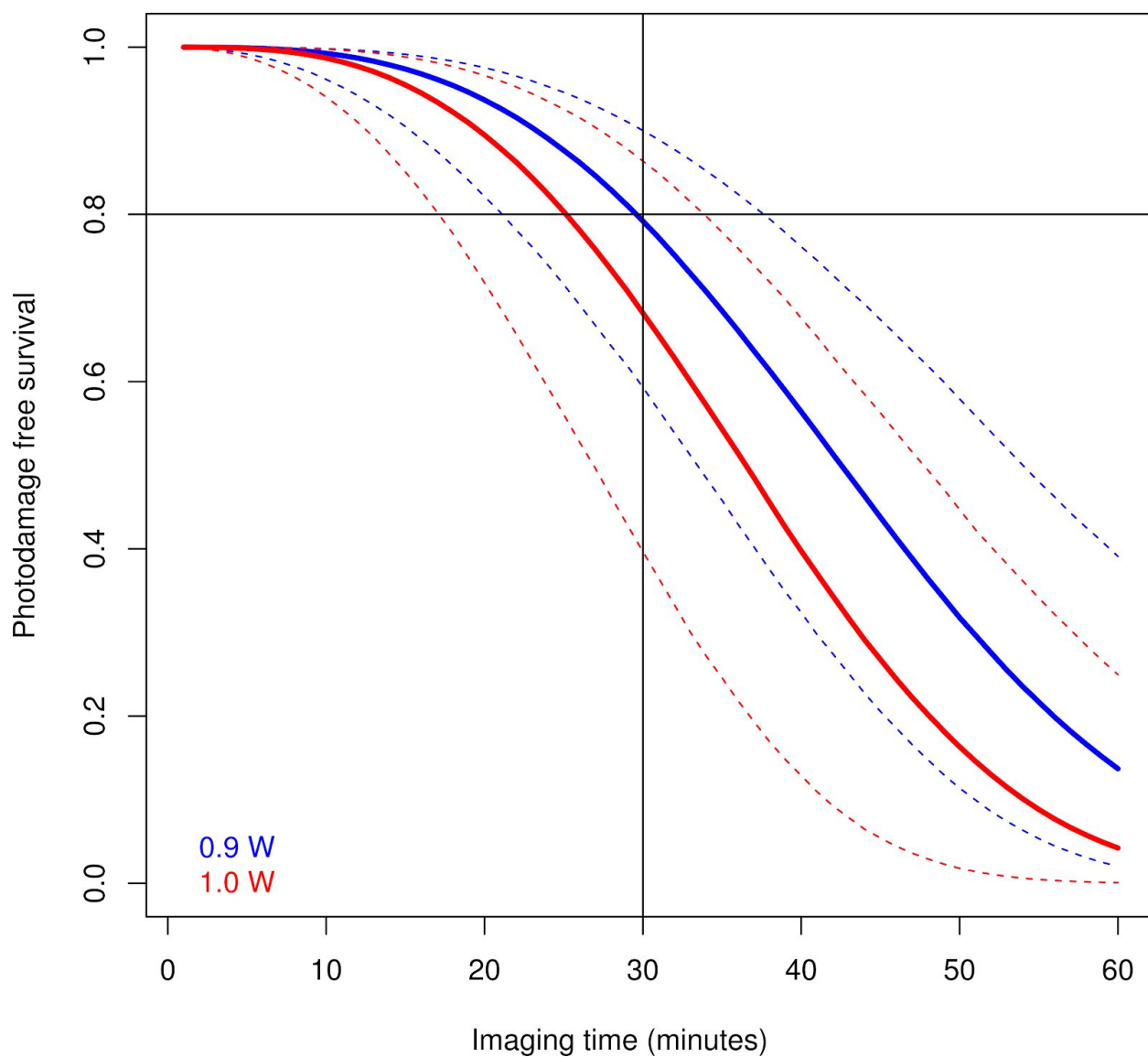
underlying specific brain states⁴⁷ and behaviors, such as circadian rhythm²⁵ or virtual-reality driven responses. Finally, the temporal resolution achieved by the system, combined with its cellular resolution, will enable a future extension of the setup with an optogenetic excitation control module, to perform real-time closed-loop control of neuronal activity.

Acknowledgements

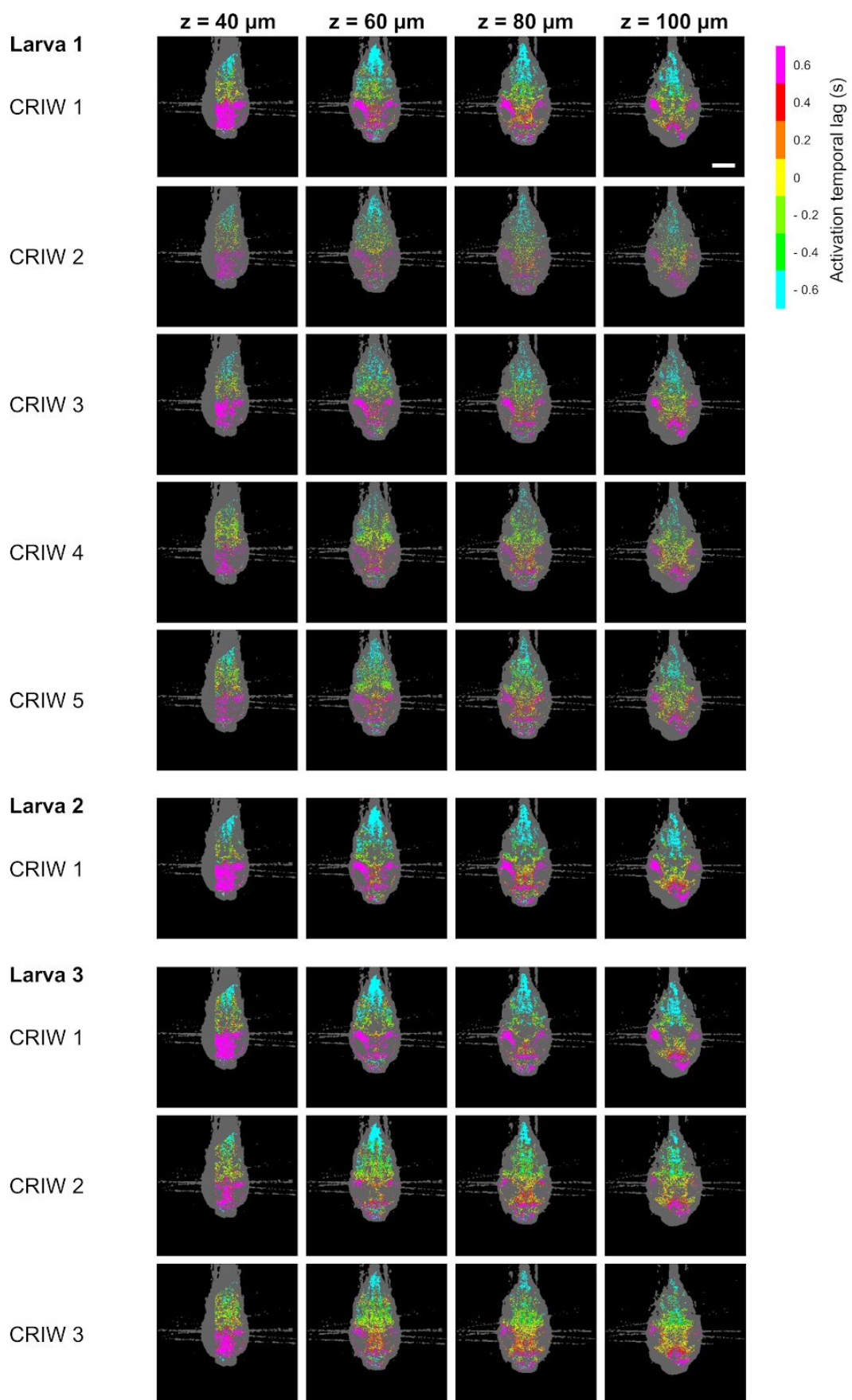
This project has received funding from the European Research Council (ERC) under the European Union's Horizon 2020 research and innovation programme (grant agreement No 692943).

We thank Dr. Luca Pesce and Dr. Vladislav Gavryusev (both from European Laboratory for Non-Linear Spectroscopy and Department of Physics and Astronomy, University of Florence). The former for his help for the detection-PSF measurements and the latter for his help with closed-loop galvanometric mirror PID controller configuration. Moreover, we thank Dr. Anna Letizia Allegra Mascaro (from European Laboratory for Non-Linear Spectroscopy and Neuroscience Institute, National Research council), Dr. Francesco Resta and Dr. Alessandro Scaglione (both from European Laboratory for Non-Linear Spectroscopy and Department of Physics and Astronomy, University of Florence) for their useful insights and suggestions. Finally, we thank Dr. Chiara Fornetto (from European Laboratory for Non-Linear Spectroscopy) for her help with the phototoxicity measures.

We acknowledge Lizzy Griffiths for zebrafish larva drawing.



Supplementary Fig. 1. Photodamage free survival curves based on posterior distributions provided by the Bayesian model as a function of the uninterrupted imaging time. Different colours indicate different excitation power levels detected at the exit of the EOM, as specified in the legend. Dashed lines indicate 90%-CI. The vertical and horizontal black lines indicate the 30 minute time frame and the 80% survival probability, respectively.



Supplementary Fig. 2. Representativeness of the aggregated colour-map of CRIWs. These colour-maps display, for each recorded CRIW event (different rows) from the different larvae, the voxels having the same lag-value (colour) as in the aggregated colour-map shown in Fig. 3A, central panel ("ICTAL"). Different dorso-ventral depths of a larva (indicated on the top, with respect to the dorsal surface) are shown across columns. Unmasked voxels with non-concordant lag values are displayed in grey. Colour code as in Fig. 3A and as specified in the colour-bar on the top-right. Scale bar: 100 μm .

Bibliography

1. Helmchen, F. & Denk, W. Deep tissue two-photon microscopy. *Nature Methods* **2**, 932–940 (2005).
2. Dombeck, D. A., Khabbaz, A. N., Collman, F., Adelman, T. L. & Tank, D. W. Imaging Large-Scale Neural Activity with Cellular Resolution in Awake, Mobile Mice. *Neuron* **56**, 43–57 (2007).
3. Keller, P. J., Schmidt, A. D., Wittbrodt, J. & Stelzer, E. H. K. Reconstruction of Zebrafish Early Embryonic Development by Scanned Light Sheet Microscopy. *Science* **322**, 1065–1069 (2008).
4. Sofroniew, N. J., Flickinger, D., King, J. & Svoboda, K. A large field of view two-photon mesoscope with subcellular resolution for in vivo imaging. *eLife* **5**, e14472 (2016).
5. Ouzounov, D. G. *et al.* In vivo three-photon imaging of activity of GCaMP6-labeled neurons deep in intact mouse brain. *Nature Methods* **14**, 388–390 (2017).
6. Chen, T.-W. *et al.* Ultrasensitive fluorescent proteins for imaging neuronal activity. *Nature* **499**, 295–300 (2013).
7. Dana, H. *et al.* High-performance calcium sensors for imaging activity in neuronal populations and microcompartments. *Nature Methods* **16**, 649–657 (2019).
8. Huisken, J., Swoger, J., Bene, F. D., Wittbrodt, J. & Stelzer, E. H. K. Optical Sectioning Deep Inside Live Embryos by Selective Plane Illumination Microscopy. *Science* **305**, 1007–1009 (2004).
9. Ahrens, M. B., Orger, M. B., Robson, D. N., Li, J. M. & Keller, P. J. Whole-brain functional imaging at cellular resolution using light-sheet microscopy. *Nature Methods* **10**, 413–420 (2013).
10. Panier, T. *et al.* Fast functional imaging of multiple brain regions in intact zebrafish larvae using Selective Plane Illumination Microscopy. *Front. Neural Circuits* **7**, (2013).

11. Dunn, T. W. *et al.* Brain-wide mapping of neural activity controlling zebrafish exploratory locomotion. *eLife* **5**, e12741 (2016).
12. Migault, G. *et al.* Whole-Brain Calcium Imaging during Physiological Vestibular Stimulation in Larval Zebrafish. *Current Biology* **28**, 3723–3735.e6 (2018).
13. Vladimirov, N. *et al.* Brain-wide circuit interrogation at the cellular level guided by online analysis of neuronal function. *Nature Methods* **15**, 1117–1125 (2018).
14. Vanwalleghem, G., Schuster, K., Taylor, M. A., Favre-Bulle, I. A. & Scott, E. K. Brain-Wide Mapping of Water Flow Perception in Zebrafish. *J. Neurosci.* **40**, 4130–4144 (2020).
15. Vladimirov, N. *et al.* Light-sheet functional imaging in fictively behaving zebrafish. *Nature Methods* **11**, 883–884 (2014).
16. Göppert-Mayer, M. Über Elementarakte mit zwei Quantensprüngen. *Annalen der Physik* **401**, 273–294 (1931).
17. Emran, F., Rihel, J., Adolph, A. R. & Dowling, J. E. Zebrafish larvae lose vision at night. *PNAS* **107**, 6034–6039 (2010).
18. Dekens, M. P. S., Foulkes, N. S. & Tessmar-Raible, K. Instrument design and protocol for the study of light controlled processes in aquatic organisms, and its application to examine the effect of infrared light on zebrafish. *PLOS ONE* **12**, e0172038 (2017).
19. Maioli, V. *et al.* Fast in vivo multiphoton light-sheet microscopy with optimal pulse frequency. *Biomed. Opt. Express*, *BOE* **11**, 6012–6026 (2020).
20. Truong, T. V., Supatto, W., Koos, D. S., Choi, J. M. & Fraser, S. E. Deep and fast live imaging with two-photon scanned light-sheet microscopy. *Nat Methods* **8**, 757–760 (2011).
21. Maruyama, A. *et al.* Wide field intravital imaging by two-photon-excitation digital-scanned light-sheet microscopy (2p-DSLM) with a high-pulse energy laser. *Biomed. Opt. Express*, *BOE* **5**, 3311–3325 (2014).

22. Zhao, M. *et al.* Cellular imaging of deep organ using two-photon Bessel light-sheet nonlinear structured illumination microscopy. *Biomed. Opt. Express*, **BOE 5**, 1296–1308 (2014).
23. Wolf, S. *et al.* Whole-brain functional imaging with two-photon light-sheet microscopy. *Nat Methods* **12**, 379–380 (2015).
24. de Vito, G. *et al.* Two-photon light-sheet microscopy for high-speed whole-brain functional imaging of zebrafish neuronal physiology and pathology. in *Neurophotonics* vol. 11360 1136004 (International Society for Optics and Photonics, 2020).
25. de Vito, G. *et al.* Two-photon high-speed light-sheet volumetric imaging of brain activity during sleep in zebrafish larvae. in *Neural Imaging and Sensing 2020* vol. 11226 1122604 (International Society for Optics and Photonics, 2020).
26. de Vito, G. *et al.* Effects of excitation light polarization on fluorescence emission in two-photon light-sheet microscopy. *Biomedical Optics Express* **11**, 4651–4665 (2020).
27. R Core Team. *R: A Language and Environment for Statistical Computing*. (R Foundation for Statistical Computing, 2015).
28. Lunn, D., Spiegelhalter, D., Thomas, A. & Best, N. The BUGS project: Evolution, critique and future directions. *Statist. Med.* **28**, 3049–3067 (2009).
29. ZFIN Feature: b4. <https://zfin.org/ZDB-ALT-980203-365>.
30. Müllenbroich, M. C. *et al.* Bessel Beam Illumination Reduces Random and Systematic Errors in Quantitative Functional Studies Using Light-Sheet Microscopy. *Front. Cell. Neurosci.* **12**, (2018).
31. Westerfield, M. *The zebrafish book: a guide for the laboratory use of zebrafish (Danio rerio)*. (Univ. of Oregon Press, 2000).
32. Turrini, L. *et al.* Optical mapping of neuronal activity during seizures in zebrafish. *Sci Rep* **7**, 1–12 (2017).
33. Galecki, A. & Burzykowski, T. *Linear Mixed-Effects Models Using R: A Step-by-Step*

- Approach*. (Springer-Verlag, 2013). doi:10.1007/978-1-4614-3900-4.
34. Kuznetsova, A., Brockhoff, P. B. & Christensen, R. H. B. lmerTest Package: Tests in Linear Mixed Effects Models. *J STAT SOFTW* **82**, (2017).
 35. Bürkner, P.-C. brms: An R Package for Bayesian Multilevel Models Using Stan. *Journal of Statistical Software* **80**, 1–28 (2017).
 36. Sancataldo, G. *et al.* Flexible Multi-Beam Light-Sheet Fluorescence Microscope for Live Imaging Without Striping Artifacts. *Front. Neuroanat.* **13**, (2019).
 37. Fahrbach, F. O., Voigt, F. F., Schmid, B., Helmchen, F. & Huisken, J. Rapid 3D light-sheet microscopy with a tunable lens. *Opt. Express*, *OE* **21**, 21010–21026 (2013).
 38. Baraban, S. C., Taylor, M. R., Castro, P. A. & Baier, H. Pentylentetrazole induced changes in zebrafish behavior, neural activity and c-fos expression. *Neuroscience* **131**, 759–768 (2005).
 39. Afrikanova, T. *et al.* Validation of the Zebrafish Pentylentetrazol Seizure Model: Locomotor versus Electrographic Responses to Antiepileptic Drugs. *PLOS ONE* **8**, e54166 (2013).
 40. Ono, J., Vieth, R. F. & Walson, P. D. Electrocorticographical observation of seizures induced by pentylentetrazol (PTZ) injection in rats. *Funct Neurol* **5**, 345–352 (1990).
 41. Randlett, O. *et al.* Whole-brain activity mapping onto a zebrafish brain atlas. *Nature Methods* **12**, 1039–1046 (2015).
 42. Kunst, M. *et al.* A Cellular-Resolution Atlas of the Larval Zebrafish Brain. *Neuron* **103**, 21-38.e5 (2019).
 43. Fisher, R. S., Scharfman, H. E. & deCurtis, M. How can we identify ictal and interictal abnormal activity? *Adv Exp Med Biol* **813**, 3–23 (2014).
 44. Winter, M. J. *et al.* 4-dimensional functional profiling in the convulsant-treated larval zebrafish brain. *Scientific Reports* **7**, 6581 (2017).
 45. Rosch, R. E., Hunter, P. R., Baldeweg, T., Friston, K. J. & Meyer, M. P. Calcium imaging

and dynamic causal modelling reveal brain-wide changes in effective connectivity and synaptic dynamics during epileptic seizures. *PLOS Computational Biology* **14**, e1006375 (2018).

46. Wolf, S. *et al.* Sensorimotor computation underlying phototaxis in zebrafish. *Nat Commun* **8**, 1–12 (2017).

47. Chicchi, L. *et al.* Reconstruction scheme for excitatory and inhibitory dynamics with quenched disorder: application to zebrafish imaging. *arXiv:2007.04370 [cond-mat, q-bio]* (2020).